High Resolution SSA Imaging using Carbon Fiber Telescopes

Ryan Swindle
Air Force Research Laboratory (AFRL/RDSM), thomas.swindle@us.af.mil
Douglas Hope
Hart Scientific Consulting International, dhope@hartsci.com
Michael Hart
Hart Scientific Consulting International, mhart@hartsci.com
Stuart Jefferies
Georgia State University, sjefferies@gsu.edu

ABSTRACT

High resolution, ground-based imagery of satellites plays an important role in space situational awareness (SSA). Current approaches generally rely on large aperture telescopes equipped with adaptive optics. These requirements place limitations on Air Force (AF) surveillance capability by restricting coverage of the sky to that which can be achieved from the small number of geographical locations where the AF has a surveillance facility. However, recent advances in carbon fiber reinforced polymer (CFRP) telescopes offer the potential for field-deployable, large aperture (>1m) telescopes for ground-based imaging of space objects. A major cost driver of a CRFP telescope is the optical quality of the primary mirror, where the cost depends on the amount of polishing and or mechanical post-processing applied to the mirror. Here we show, using both numerical simulations and real data, that a CFRP telescope with significant optical aberration can be used for high-resolution imaging if the telescope is equipped with a wavefront sensor (WFS), and the recorded image and WFS data are processed, as in this case, using the Daylight Object Restoration Algorithm (DORA).

1. INTRODUCTION

Novel ultra-lightweight mirrors are now being manufactured in various ways, including (but not limited to): CFRP [1, 2], SiC/C-SiC [3], or even thinned, actuated fire-polished glass [4]. Whether destined for a ground- or a space-based application, each has its pros and cons. For a ground-based, large aperture, 24/7 SSA telescope, CFRP has particularly interesting advantages: higher thermal conductivity, easier scalability, and coefficient of thermal expansion (CTE) matching to CFRP telescope structures. That said, its manufacturing process for large optics has seen a relatively slow evolution towards perhaps the end goal of diffraction-limited performance; the surface figure accuracy is overall questionable (see Sec. 2). However, other features like surface roughness [1] and long-term stability [5] appear to be meeting specs.

In this experiment, we begin to evaluate the imaging limitations of current CFRP surface figure error when the data is post-processed, in this case, with an algorithm that aims to solve for both dynamic *and static* layers of added phase error (DORA; see Sec. 3); more importantly, the algorithm is already being investigated and suggested for 24/7 use on ground-based, large aperture imaging systems. To this end, we analyze simulated data (see Sec. 4) as well as on-sky imaging and WFS data (see Sec. 5) that have added static aberrations. Calibrating these aberrations – often in the form of so-called non-common path errors – is an important method for obtaining high contrast, high spatial resolution imaging. Phase retrieval [6] and diversity [7] employ multiple, defocused PSFs usually from an artificial source. Some other procedures employ multiple deformable mirrors [8] or additional WFSs beyond the adaptive optics (AO) system [9]. Using the imager and WFS data themselves is an intriguing alternative and adds some simplicity to newly developing meter-class SSA telescopes.

2. A SAMPLE 1M-CLASS CFRP TELESCOPE

The common process for manufacturing large aperture CFRP optics begins with the polishing of a convex, glass mandrel of equivalent aperture and negative shape. A unique matrix of CFRP plies is then adhered to the mandrel with a resin and cured in an autoclave, producing a front *facesheet*. The remaining material (e.g. core support structure and back facesheet) is attached, with the entire mirror then removed from the mandrel and coated (see [1,

10] for more details). The immediate result is a mirror that is mandrel-limited in terms of surface figure error – in the absence of additional figure post-processing – but with order ~50% reduced weight, near zero CTE, and the potential for significant cost savings as the same mandrel can be used to replicate many, cheaper CFRP optics. The mandrel surface figure – and in some cases, the fiber and/or core support structure print-through – then determine the achievable image resolution and contrast in an assembled telescope.

Attempts at CFRP optic replication in the $D \lesssim 0.5$ m class appear to yield near diffraction-limited wavefront quality from the primary mirror (i.e. for both flat and curved mandrels; see [11] for a summary). However, larger apertures ($D \gtrsim 1$ m) are either in less demand or are not meeting this same performance in visible light applications (or both), at least according to the literature. We know that at least the latter is true for an off-the-mandrel CFRP optic, as evident by limitations in meter-class convex mandrel fabrication (see Fig. 9 of [12], reproduced here in Fig. 1 out to the full 1 m aperture from vendor provided data). This 1 m mandrel has a 280 nm RMS surface figure error with significant contributions from a turned-down edge, which is not surprising but is also likely to limit high spatial frequency content in the final image; it is worth noting that the inner 0.8 m is polished considerably better at 32 nm RMS. We investigate this particular mandrel's limitations on image quality in the next two sections.

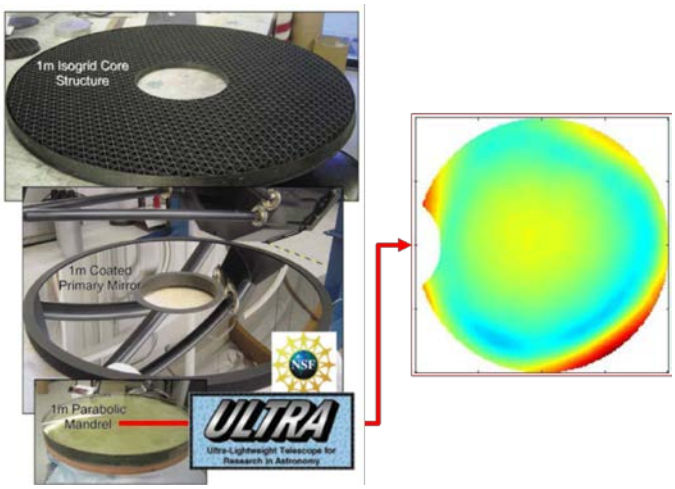

Fig. 1. (*Left*) Characteristic CFRP primary mirror structure (top), bonded to the CFRP replication from a convex glass mandrel (bottom); figure taken from [10]. (*Right*) Profilometer measurement of 1 m convex mandrel that can be used to replicate a [concave] CFRP facesheet. The total scale is 2042 nm P-V (280 nm RMS), and a chip is being masked out on the left hand side of the image.

3. HIGH RESOLUTION WAVEFRONTS FROM DORA

Such a 1m-class telescope is initially destined for ground-based imaging and is therefore subject to various sources of atmospheric turbulence, parameterized throughout this paper by the coherence length r_0. Ideally, its added optical aberrations would not induce premature failure of a particular image post-processing algorithm's ability to converge on a point-spread function. With that in mind, we chose the Daylight Object Restoration Algorithm (DORA; [13, 14]) – which explicitly targets image restoration in high D/r_0 regimes – to attempt recovery and removal of the added CFRP primary mirror wavefront error.

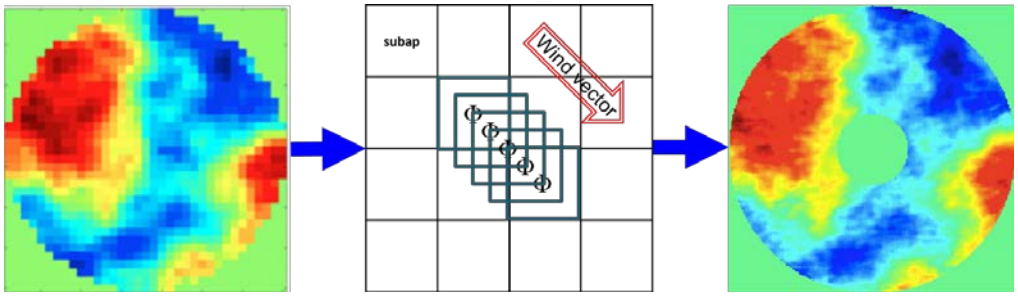

Fig. 2. (*Left*) Simulated turbulence ($D/r_0=70$) observed with a 32x32 subaperture Shack-Hartmann WFS. (*Center*) Schematic image of WFS with frozen phase advecting across subapertures. (*Right*) The same turbulence scenario observed and post-processed with 40 frames of a τ_{FFM}~100 ms frozen flow. The improved sampling is evident in the region of larger phase slopes.

DORA implements the technique of deconvolution from wavefront sensing while also exploiting the frozen flow hypothesis among other things (see [13, 14] for details). It targets the critical high spatial frequencies of the wavefront by modeling the atmosphere as well-separated layers of frozen turbulence with different velocities (the frozen flow model, FFM). The result is a higher resolution estimate of the wavefront than could be naively obtained with its Shack-Hartmann wavefront sensor sampling alone (see Fig. 2, for example). This experiment proceeded by testing whether DORA can utilize the frozen flow to its advantage in recovering a separate, high resolution estimate of the CFRP primary mirror. The first approach was simple: can DORA model the static aberration as a zero-velocity layer in the FFM? Due to the limited size of the FFM (τ_{FFM}~100 ms), an insufficient number of frames is available for a robust static layer estimate; in turn, this negatively impacts estimates of the dynamic turbulent layers, as well. So, we focus on the second approach to calculating static phases $\hat{\varphi}_s(\vec{x})$, which is two-tiered: 1) calculate the mean value of the WFS slope data, $\langle \nabla_x \varphi(\vec{x}) \rangle$ and $\langle \nabla_y \varphi(\vec{x}) \rangle$; and 2) compute a FFM including those values. Step 1 estimates the *xy* gradients of the static aberration, while step 2 effectively interpolates this estimate to a *higher resolution (HR)* than naively achieved from the WFS itself. Or, in qualitative terms:

$$FFM\{\langle \nabla_x \varphi(\vec{x}) \rangle, \langle \nabla_y \varphi(\vec{x}) \rangle\} \rightarrow \{\nabla_x^{HR} \varphi(\vec{x}), \nabla_y^{HR} \varphi(\vec{x})\} \rightarrow \hat{\varphi}_s(\vec{x})$$

Ideally, we would employ a large number of subapertures (e.g. 32) across the pupil; this would improve sampling near the edges of the mirror where the mandrel polishing lap is more difficult to control. However, we end up fighting both lower light levels and increased diffraction spot sizes, which challenge wavefront and centroid estimates and compromise accuracy of the wavefront determination. It is this two-step approach above that allows high resolution sampling at a lower number of subapertures. Fig. 3 shows the resulting estimate of the static aberration layer from a 14x14 and 35x35 subaperture Shack-Hartmann WFS as compared to a simulated profilometer measurement of the mirror. As expected, the 35x35 subaperture measurement provides more overall definition and contrast, but as we will show in Sec. 4, the estimate from 14x14 sampling is sufficient to restore imagery in even moderate atmospheric turbulence.

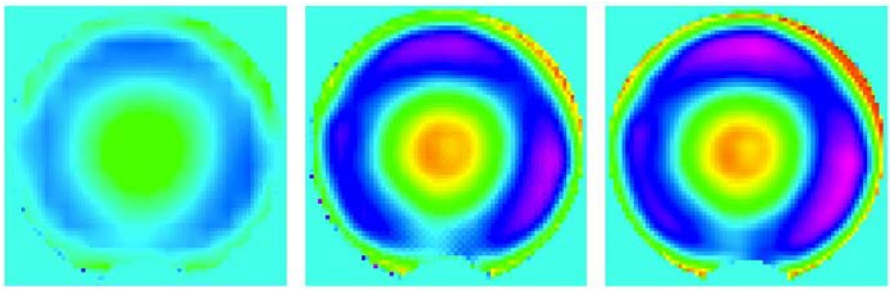

Fig. 3. (*Left*) Estimate of the static aberration (CFRP) layer after interpolation from a FFM with a 14x14 subaperture WFS. (*Center*) Estimate with a higher sampling density of 35x35. (*Right*) Measurement of the static aberration layer from a profilometer; this measurement was used to create synthetic PSFs for the simulations of Sec. 4.

4. LEO SIMULATIONS & RESULTS

We added the profilometer surface maps as phase errors to simulated, Kolmogorov atmospheric turbulences across D/r_0=5, 10, 25, 30, and 40. For the FFM, we assumed a two-layer wind model after the observations of [15] above Haleakalā. These dynamic and static phase errors were then convolved with diffraction-limited (*D*=1 m) images of the Hubble Space Telescope (HST).

Fig. 4 shows images of HST in D/r_0=10 turbulence, the CFRP surface figure shown in Fig. 1, a wavelength of 750 nm, and exposure times of 2 ms for both the WFS and the imager. The results shown here assume a conservative 14x14 subaperture WFS geometry. The mean value of the WFS slope data was estimated over 2560 frames (i.e. 5 s of data at 512 fps), and 11 frames were used to compute a FFM.

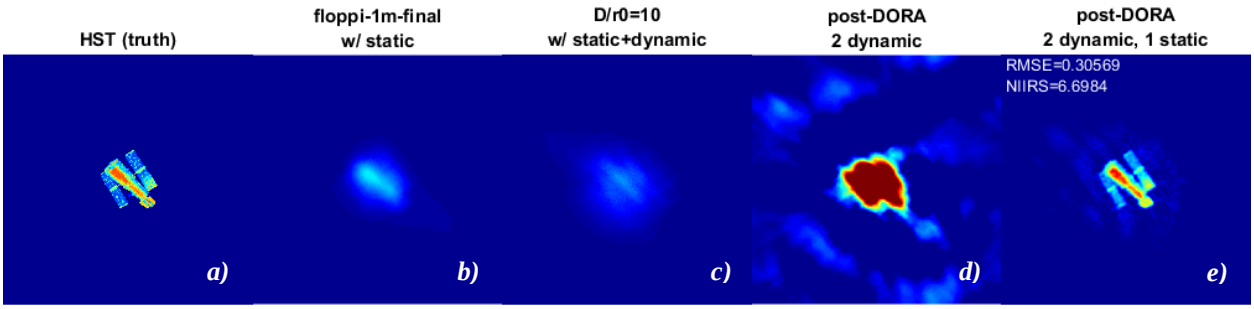

Fig. 4. Images of HST after various aberration and/or processing stages. *a*) diffraction-limited (truth) image; *b*) the static aberration from Fig. 1 added to *a*); *c*) atmospheric turbulence (D/r_0=10) per the model described above added to *b*); *d*) a DORA restoration if the FFM assumes non-zero velocity aberration layers *only* (for which it finds two); *e*) a DORA restoration if the aberration layers are modeled and found vis-à-vis the approach summarized in Sec. 3. RMSE is the root mean squared error between panels *a*) and *e*), and the NIIRS image quality metric is computed via the ITIQUE framework [16], where NIIRS=6-7 (out of 9) is considered *good*. All images are on the same scale.

The diffraction-limited image of HST (panel *a*) allows resolution of the telescope body and solar panel substructures with appreciable contrast. This is almost entirely lost upon addition of the mandrel-limited CFRP mirror aberration (panel *b*) and certainly so with addition of the turbulent atmosphere (panel *c*). If a DORA with FFM restoration is attempted as normal (modeling atmospheric turbulence *only*), then a failure results with all likeness of HST lost (panel *d*). However, accounting for the static layer's presence prior to generating a FFM allows successful restoration of the satellite (panel *e*) with even the smallest solar panel substructures being resolvable, although with slightly reduced constrast, at least at a D/r_0=10 turbulence level. To this point, the static aberration does lower the D/r_0 threshold for successful restoration for an object like HST (m_V~2.5), which in our experience is restorable out to D/r_0~100 [13] for the two-layer atmosphere typical of Haleakalā, albeit for a 3.6 m aperture telescope with 30x30 subapertures in that study. For our 1 m aperture here, reasonable restorations are achieved out to D/r_0=25 (see Fig. 5), which is worse than even the median daytime seeing conditions atop Haleakalā [17].

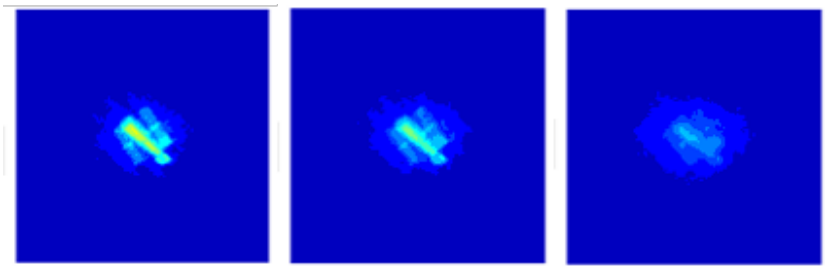

Fig. 5. Images of HST in D/r_0=25 (*left*), 30 (*center*), and 40 (*right*) turbulence and the static aberration from Fig. 3, displayed on the same scale as in Fig. 4. Images processed with DORA and a high-resolution model of the static aberration layer.

5. AEOS EXPERIMENT & RESULTS

The next step appeared to be an on-sky demonstration. In lieu of a CFRP telescope manufactured from the mandrel in Fig. 1, we used the 941 actuator deformable mirror (DM) on the 3.6 m Advanced Electro-Optical System (AEOS) telescope adaptive optics system atop Haleakalā. Applying the static aberration at this location mimics that of the primary mirror mandrel since both mirrors are optically conjugate. This DM has 32 actuators spaced across the diameter of the clear aperture, where the result of mapping the mandrel surface figure onto the coarser DM sampling is shown in Fig. 6 along with an image of the DM surface taken with a Zygo. The surface WFE is ~2λ P-V, and despite the undersampling near the edges, the global shape appears sufficiently well-represented.

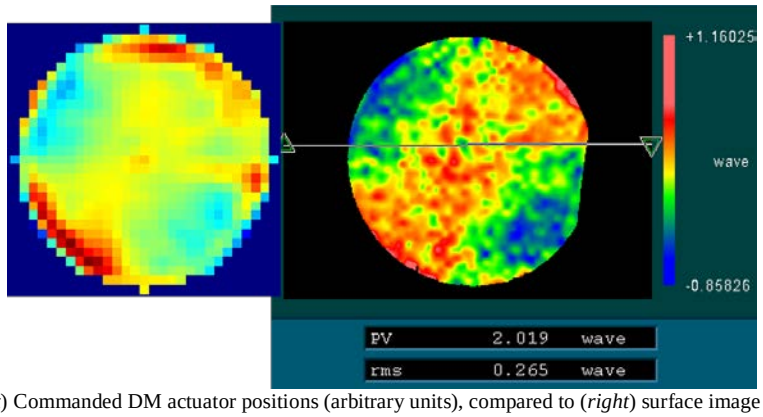

Fig. 6. (*Left*) Commanded DM actuator positions (arbitrary units), compared to (*right*) surface image from Zygo.

Several stars and LEO satellites were observed in this configuration of the adaptive optics system, using the 32x32 subaperture WFS sensing at λ=540-700 nm and 945 fps and an imager sensing in the Sloan i' band. For each object/pass, the experiment then proceeded as follows: 1) close the AO loop and record simultaneous, IRIG time stamped WFS and imager frames; this serves as an on-sky truth reference; 2) open the AO loop, flatten the DM, and record; this sets up a nominal (i.e. atmosphere *only*) DORA restoration as a diagnostic tool; and 3) add the static offset to the DM, keep the loop open, and record. We presume that the atmospheric turbulence does not change significantly in between each step, and this assumption appears well-justified. For example, r_0 varied from 11.7 to 12.1 between steps 2 and 3 for star HR 5477 below and was consistently around D/r_0~30 throughout the night.

To process each data set, we first compute wavefront gradients and image centroids to determine any synchronization delays between the two channels, the scaling of the wavefront *xy* gradients, and their relative orientations. We then compute the spatio-temporal autocorrelation of the WFS measurements and use this to estimate the number of wind layers. All of this and relevant sensor metadata is then fed into DORA and processed according to the outline given in [14]. Fig. 7 shows images of the binary star system HR 5477, where the FFM required 57 frames to allow the slowest measured wind layer to propagate across a full subaperture.

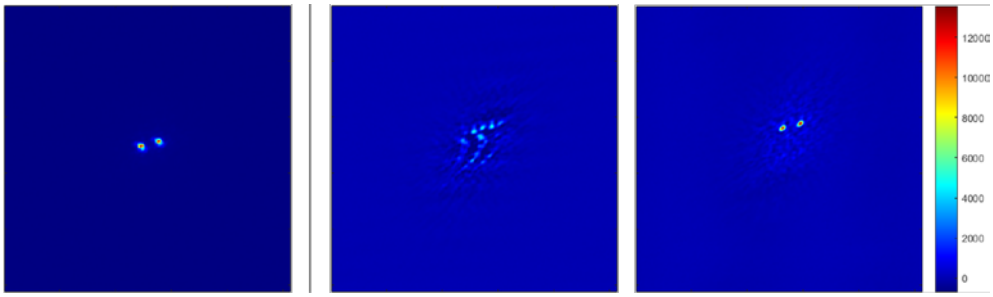

Fig. 7. (*Left*) Closed-loop AO image of HR 5477. (*Center*) Post-processed image without accounting for ~2λ of static WFE, compared to (*right*) the same data set, post-processed with the same parameters, except allowing DORA to model a static phase error layer. The *center* and *right* images are displayed on the same arbitrary scale, but the closed-loop AO image is not (i.e. no photometric calibration is applied).

The improvement in image resolution is clearly seen in the right panel of Fig. 7. Compared to the closed-loop AO image of the binary system, DORA is doing a remarkable job at removing the additional ~2λ (P-V) of added static phase error. Improvement can also be seen in the images of Cosmos 1606 shown in Fig. 8. This object culminated at a favorable 70 degrees elevation during evening terminator and presents several radially distinct solar panels (*left*) as well as some spatial diversity near its center. However, between steps 1 and 3 of the observation (about 3 min), the satellite pose changed sufficiently to prevent a comparison between the closed-loop AO and DORA processed imagery. Note, both the star and satellite were observed during a D/r_0~30 turbulence level which, according to our simulations, is near the restoration limit under this amount of phase error.

The Cosmos 1606 data, though less dramatically improved than the stellar data, do reveal finer structures in the object after accounting for the static layer. The extended nature of the object likely contributes to this effect, in that the more severe blurring (i.e. mixing of signal in the image data from different parts of the object) changes the shape of the error surface that DORA searching across: there is no well-defined global minimum. This effect combines

with compromised WFS linearity and degraded WFS spot centroiding in the presence of photon and detector noise to limit the quality of the image restoration at these turbulence levels. Nonetheless, the FFM – when supplemented with a simple estimate of the static phases – adds robustness to the measurement of a severely aberrated PSF. And this appears to mitigate the effects of, for example, surface figure errors from collecting apertures.

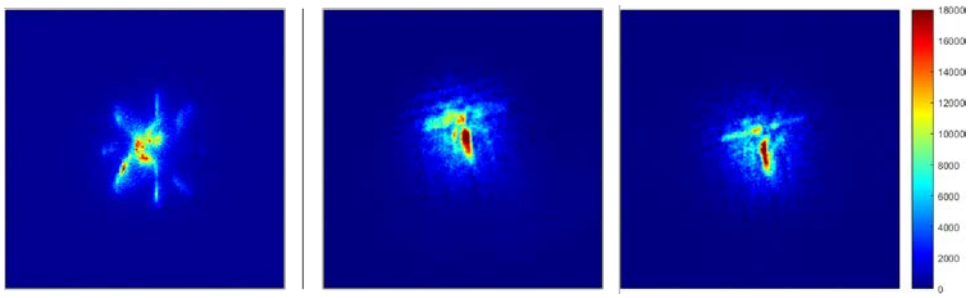

Fig. 8. (*Left*) Closed-loop AO image of Cosmos 1606. (*Center*) Post-processed image without accounting for ~2λ of static WFE, compared to (*right*) the same data set, post-processed with the same parameters, except allowing DORA to model a static phase error layer. The *center* and *right* images are displayed on the same arbitrary scale, but the closed-loop AO image is not (i.e. no photometric calibration is applied).

6. FUTURE DIRECTION

These results are encouraging and have near term applications for calibrating non-common path errors. But in the interest of fielding ultra-lightweight, large aperture optics, we are currently commissioning a 1 m CFRP telescope from the mandrel of Fig. 1. Subsequent testing would also include the added effects of, e.g., residual ply structure and core print-through. And so with the general absence of experiments on ground-based, large aperture telescopes with CFRP optics in the literature, we hope to shed some light on their utility for SSA imaging.

7. REFERENCES

1. Romeo, R. and Martin, R., "Progress in 1m-class lightweight CFRP composite mirrors for the ULTRA telescope", *SPIE*, Vol. 6273, 2006.
2. Thompson, S., et al, "Towards a large, lightweight mirror for AO – Development of a 1 m Ni coated CFRP mirror", *SPIE*, Vol. 7018, 2008.
3. Matson, L., et al, "Silicon Carbide Technologies for Lightweighted Aerospace Mirrors", *AMOS*, 2008.
4. Kuhn, J., et al, "Looking Beyond 30m-class Telescopes: The Colossus Project", *SPIE*, Vol. 9145, 2014.
5. Romeo, R., Martin, R., and Bollweg, K., "Discussions on radiation and space environment exposure of replicated optical mirrors produced from carbon composites", *SPIE*, Vol. 9616, 2015.
6. Burruss, R., et al, "Demonstration of on sky contrast improvement using the Modified Gerchberg-Saxton algorithm at the Palomar Observatory", *SPIE*, Vol. 7736, 2010.
7. Mugnier, L, Blanc, A., and Idier, J., "Phase Diversity: a Technique for Wave-Front Sensing and for Diffraction-Limited Imaging", *Advances in Imaging and Electron Physics*, Vol. 141, 2006.
8. Pueyo, L. and Norman, C., "High-Contrast Imaging with an Arbitrary Aperture: Active Compensation of Aperture Discontinuities", *ApJ*, Vol. 769, 2013.
9. N'Diaye, M., et al, "Calibration of quasi-static aberrations in exoplanet direct-imaging instruments with a Zernike phase-mask sensor", *A&A*, Vol. 555, 2013.
10. Romeo, R., et al, "Final assembly of the ULTRA 1-m carbon fiber optical telescope", *SPIE*, 6665, 2007.
11. Liang, X., et al, "The development of high precision carbon fiber composite mirror", *SPIE*, Vol. 9683, 2016.
12. Wilcox, C., et al, "The meter-class carbon fiber reinforced polymer mirror and segmented mirror telescope at the Naval Postgraduate School", *SPIE*, Vol. 9354, 2015.
13. Jefferies, S. and Hart, M., "Deconvolution from wave front sensing using the frozen flow hypothesis", *Optics Express*, Vol. 19, 1975-1984, 2011.
14. Hope, D. et al, "Robust image restoration for ground-based space surveillance", *AMOS*, 2013.
15. Rimmele, T., "Haleakala turbulence and wind profiles used for adaptive optics performance modeling", *ATST Project Document RPT-0300*, 1996.
16. Gerwe, D., Luna, C., and Calef, B., "Application of the ITIQUE Image Quality Modeling Metric to SSA Domain Imagery", *AMOS*, 2012.
17. Bradford, W., "Maui4: a 24 hour Haleakala turbulence profile", *AMOS*, 2010.